

Dartmouth College

Dartmouth Digital Commons

Dartmouth Scholarship

Faculty Work

5-2-2013

Continuous Correction of Differential Path Length Factor in Near-Infrared Spectroscopy

Tanveer Talukdar
Dartmouth College

Jason H. Moore
Dartmouth College

Solomon G. Diamond
Dartmouth College

Follow this and additional works at: <https://digitalcommons.dartmouth.edu/facoa>



Part of the [Engineering Commons](#), and the [Medicine and Health Sciences Commons](#)

Dartmouth Digital Commons Citation

Talukdar, Tanveer; Moore, Jason H.; and Diamond, Solomon G., "Continuous Correction of Differential Path Length Factor in Near-Infrared Spectroscopy" (2013). *Dartmouth Scholarship*. 3719.
<https://digitalcommons.dartmouth.edu/facoa/3719>

This Article is brought to you for free and open access by the Faculty Work at Dartmouth Digital Commons. It has been accepted for inclusion in Dartmouth Scholarship by an authorized administrator of Dartmouth Digital Commons. For more information, please contact dartmouthdigitalcommons@groups.dartmouth.edu.

Journal of Biomedical Optics

SPIDigitalLibrary.org/jbo

Continuous correction of differential path length factor in near-infrared spectroscopy

Tanveer Talukdar
Jason H. Moore
Solomon G. Diamond



SPIE

Continuous correction of differential path length factor in near-infrared spectroscopy

Tanveer Talukdar,^a Jason H. Moore,^b and Solomon G. Diamond^a

^aThayer School of Engineering at Dartmouth, Hanover, New Hampshire

^bGeisel School of Medicine at Dartmouth, Department of Genetics, Institute for Quantitative Biomedical Sciences, Lebanon, New Hampshire

Abstract. In continuous-wave near-infrared spectroscopy (CW-NIRS), changes in the concentration of oxyhemoglobin and deoxyhemoglobin can be calculated by solving a set of linear equations from the modified Beer-Lambert Law. Cross-talk error in the calculated hemodynamics can arise from inaccurate knowledge of the wavelength-dependent differential path length factor (DPF). We apply the extended Kalman filter (EKF) with a dynamical systems model to calculate relative concentration changes in oxy- and deoxyhemoglobin while simultaneously estimating relative changes in DPF. Results from simulated and experimental CW-NIRS data are compared with results from a weighted least squares (WLSQ) method. The EKF method was found to effectively correct for artificially introduced errors in DPF and to reduce the cross-talk error in simulation. With experimental CW-NIRS data, the hemodynamic estimates from EKF differ significantly from the WLSQ ($p < 0.001$). The cross-correlations among residuals at different wavelengths were found to be significantly reduced by the EKF method compared to WLSQ in three physiologically relevant spectral bands 0.04 to 0.15 Hz, 0.15 to 0.4 Hz and 0.4 to 2.0 Hz ($p < 0.001$). This observed reduction in residual cross-correlation is consistent with reduced cross-talk error in the hemodynamic estimates from the proposed EKF method. © 2013 Society of Photo-Optical Instrumentation Engineers (SPIE) [DOI: 10.1117/1.JBO.18.5.056001]

Keywords: biomedical optics; spectroscopy; optical properties; real-time imaging; signal processing.

Paper 12714R received Nov. 5, 2012; revised manuscript received Mar. 16, 2013; accepted for publication Mar. 21, 2013; published online May 2, 2013.

1 Introduction

In functional near-infrared spectroscopy (fNIRS) studies, cerebral blood volume and blood oxygenation changes are studied as indicators of brain activity. Hemodynamics are quantified based on localized changes in the concentrations of oxyhemoglobin (HbO) and deoxyhemoglobin (HbR). Three different classes of NIRS instrumentation are used to measure cerebral hemodynamics, and each have certain advantages and disadvantages. Time-domain NIRS (TD) and frequency domain NIRS (FD) are capable of providing absolute quantification of hemodynamics.¹⁻³ TD provides superior depth resolution by tracking the time of flight of photons.⁴ However, the complexity of TD and FD systems make them more costly for scale up to high-density measurement probes⁵ and whole head neuroimaging.⁶ The instrument of choice for high-density neuroimaging applications with NIRS is continuous-wave (CW).

With CW-NIRS systems, the attenuation of light is measured at multiple wavelengths between source and detector optodes that are separated by a few centimeters on the scalp. The change in light absorption or optical density ΔOD_λ for a given wavelength, λ , is the negative logarithm of the ratio of the detected light at a given time t_2 relative to the detected light at a reference time t_1

$$\Delta OD_\lambda = -\log_{10} \left[\frac{I(t_2)}{I(t_1)} \right]. \quad (1)$$

Changes in HbO and HbR can be calculated by solving a set of linear equations based on the modified Beer-Lambert Law (MBLL):⁷

$$\Delta OD_\lambda = \epsilon_{\text{HbO},\lambda} \cdot \text{DPF}_\lambda \cdot d \cdot \Delta \text{HbO} + \epsilon_{\text{HbR},\lambda} \cdot \text{DPF}_\lambda \cdot d \cdot \Delta \text{HbR}, \quad (2)$$

where ΔHbO and ΔHbR represent changes in concentration of HbO and HbR, respectively, and $\epsilon_{\text{HbO},\lambda}$ and $\epsilon_{\text{HbR},\lambda}$ are the molar extinction coefficients that specify how strongly HbO and HbR absorb light at a given wavelength. The product $\text{DPF}_\lambda \cdot d$ is the mean optical path length, where d is the source-detector separation distance and DPF_λ is the wavelength-dependent differential path length factor. DPF_λ effectively scales the linear distance between the source and detector optodes to account for the increased distance that light travels due to scattering and absorption effects within the tissue.

Unlike TD or FD, CW-NIRS cannot be used to determine DPF_λ . Typically, the assumed DPF_λ values used in CW-NIRS analysis are obtained from prior studies of healthy subjects and range from three to six.^{2,8} However, DPF_λ can vary between subjects due to differences in the anatomical structure and tissue composition of the brain. Morphological changes in the brain induced by aging or neurological disorders can affect the optical properties of brain tissue, altering DPF_λ values.⁹ Furthermore, DPF_λ used in the MBLL is assumed constant for a specific wavelength and cannot account for partial volume effects that arise from assuming global changes in the concentrations of HbO and HbR in a brain volume consisting of multiple layers

Address all correspondence to: Tanveer Talukdar, Thayer School of Engineering at Dartmouth, 14 Engineering Drive, Hanover, New Hampshire 03755. Tel: 603-646-1311; Fax: 603-646-0151; E-mail: tanveer@dartmouth.edu

of tissue.¹⁰ Studies have shown that skull thickness and the cerebrospinal fluid (CSF) in the head can affect the mean optical path length and hence DPF_λ values.^{11,12} The reason this is a problem is that systematic errors in DPF_λ lead to systematic errors in the quantification of cerebral oxygenation levels. In this work, we propose a method for calculating changes in the concentration of HbO and HbR while continuously correcting for systematic errors in DPF_λ .

2 Theoretical Formalism

CW-NIRS is an increasingly important tool for clinical monitoring and for diagnosis of neurological disorders. However, DPF_λ values cannot be known in advance in such patients. Efforts have been made to estimate mean optical path lengths in infants¹³ as well as in patients undergoing cardiopulmonary bypass.¹⁴ Having knowledge of DPF_λ values significantly improves the accuracy of calculated cerebral hemodynamics, which are important in the clinical evaluation of patients with stroke or brain injury.^{15,16}

When inaccurate DPF_λ values are used in the MBL, the calculated concentration changes in ΔHbO and ΔHbR become inaccurate in two ways. The first type of inaccuracy is a loss of the absolute scale on the results; the second type of inaccuracy is called cross talk, which is when ΔHbO become contaminated by ΔHbR and vice versa. From a mathematical perspective, the errors C in ΔHbO and ΔHbR are given by:

$$C_{\Delta\text{HbO}} = \Delta\text{HbO} - \Delta\text{HbO}^* \quad (3)$$

$$C_{\Delta\text{HbR}} = \Delta\text{HbR} - \Delta\text{HbR}^*, \quad (4)$$

where ΔHbO and ΔHbR represent solutions obtained from using inaccurate DPF_λ values, and the exact solutions that would have been obtained from using the correct DPF_λ values are ΔHbO^* and ΔHbR^* . Scale errors arise when the DPF_λ values are systematically too high or too low due to a multiplicative scale factor S and cross-talk errors arise when the DPF_λ values are shifted relative to one another due to an offset term ΔDPF_λ :

$$\text{DPF}_\lambda^* = S(\text{DPF}_\lambda - \Delta\text{DPF}_\lambda). \quad (5)$$

Pure scale errors result when $S \neq 1$ and pure cross talk errors occur when $S = 1$ and $\Delta\text{DPF}_\lambda \neq 0$ for all but one of the wavelengths. In NIRS spectroscopic calculations involving multiple wavelengths, the errors C in ΔHbO and ΔHbR can be computed as:

$$\mathbf{C} = \begin{bmatrix} C_{\Delta\text{HbO}} \\ C_{\Delta\text{HbR}} \end{bmatrix} = [\mathbf{A}^\dagger - \mathbf{A}^{*\dagger}] \mathbf{Y}, \quad (6)$$

where \mathbf{Y} is a vector containing ΔOD_λ measurements and \mathbf{A}^\dagger and $\mathbf{A}^{*\dagger}$ are the Moore–Penrose pseudoinverses. The matrix \mathbf{A} containing inaccurate path lengths is defined as:

$$\mathbf{A} = \begin{bmatrix} L_{\lambda_1} & 0 & \dots & 0 \\ 0 & L_{\lambda_2} & & \vdots \\ \vdots & & \ddots & 0 \\ 0 & \dots & 0 & L_{\lambda_N} \end{bmatrix} \begin{bmatrix} \varepsilon_{\Delta\text{HbO},\lambda_1} & \varepsilon_{\Delta\text{HbR},\lambda_1} \\ \varepsilon_{\Delta\text{HbO},\lambda_2} & \varepsilon_{\Delta\text{HbR},\lambda_2} \\ \vdots & \vdots \\ \varepsilon_{\Delta\text{HbO},\lambda_N} & \varepsilon_{\Delta\text{HbR},\lambda_N} \end{bmatrix} = \mathbf{L}\mathbf{E}, \quad (7)$$

which is composed of a diagonal path length matrix \mathbf{L} and a matrix of extinction coefficients \mathbf{E} . The accurate model matrix \mathbf{A}^* is composed of scalar factor S , a diagonal matrix $(\mathbf{L} + \Delta\mathbf{L})$ and the matrix \mathbf{E} , where $\Delta\mathbf{L}$ contains the offset terms for all but the N 'th mean optical path length. The scalar factor and offset terms fully account for the inaccurately assumed DPF_λ values:

$$\mathbf{A}^* = S(\mathbf{L} + \Delta\mathbf{L})\mathbf{E}, \quad (8)$$

$$\Delta\mathbf{L} = \begin{bmatrix} \Delta L_{\lambda_1} & 0 & \dots & 0 \\ 0 & \Delta L_{\lambda_2} & & \vdots \\ \vdots & & \ddots & 0 \\ 0 & \dots & 0 & \Delta L_{\lambda_N} \end{bmatrix}, \quad (9)$$

where $\Delta L_{\lambda_N} = 0$ so that the scale error and cross-talk error effects are separable. The objective of the present work is to reduce the cross talk errors in ΔHbO and ΔHbR using an algorithm that can continuously correct for offsets in DPF_λ during CW-NIRS spectroscopic calculations. Scale factor errors cannot be corrected by the proposed method.

Several methods based on numerical and analytical approaches are already available for calculating DPF_λ in simulation. These methods typically rely on modeling light transport in the head using the radiative transport equation (RTE). The diffusion equation, which is derived from the P_1 approximation to the RTE^{17,18} can accurately describe photon transport in a highly scattering medium. However, in a low scattering media like CSF, the diffusion approximation does not hold. Analytical solutions to the diffusion equation, which can be obtained for simple geometries¹⁹ are difficult to solve in complex geometries like the head. Instead, numerical approaches like the finite element method (FEM) are preferred. Another numerical approach is the FEM based Monte Carlo (MC) technique.^{20–22} Although computationally expensive,²³ FEM based MC has the advantage that it can handle complex geometries like the head and can be used to solve the full RTE. The major disadvantages of simulation approaches to calculating DPF_λ values are inaccuracies in FEM representations of head anatomy and a lack of knowledge of the true optical properties in the mesh elements. Therefore, DPF_λ values obtained from simulation methods are likely to be different from the actual values, which can lead to cross-talk error in the calculated ΔHbO and ΔHbR .^{10,22,24} This motivates the need for experimental methods of calculating relative DPF_λ values from CW-NIRS data.

In the present work, we focus on calculating relative offsets in differential path length factors (DPF_λ) at wavelengths of 690, 785, and 830 nm with respect to a DPF_λ value at 808 nm that is held fixed ($\Delta\text{DPF}_{808} = 0$). We apply the extended Kalman filter (EKF) to calculate the ΔDPF_λ values and the changes in concentration of HbO and HbR. Since ΔDPF_λ is a relative correction, the calculated ΔHbO and ΔHbR are corrected relative to one another but not corrected to absolute scales. The absolute accuracies of the calculated ΔHbO and ΔHbR values are determined by the *a priori* value of DPF_λ at 808 nm.

3 Dynamic State Estimation Using the EKF Algorithm

The EKF algorithm operates on a state-space dynamical system that consists of an observation model and a process model. In our case, the observation model is based on the MBLL and is derived by relating ΔOD_{λ} to the state variables ΔDPF_{λ} , ΔHbO , and ΔHbR . The subscripts j and k are introduced in the equations below to specify the source-detector pair and the discrete time step, respectively. The MBLL-based observation model in matrix form is:

$$\mathbf{Y}_{j,k} = \mathbf{H}_{j,k} \mathbf{X}_{j,k} + \mathbf{v}_{j,k}. \quad (10)$$

In Eq. (10), $\mathbf{X}_{j,k}$ is a vector containing state variables that we want to calculate using the EKF algorithm:

$$\mathbf{X}_{j,k} = \begin{bmatrix} \Delta HbO_{j,k} \\ \Delta HbR_{j,k} \\ \Delta DPF_{\lambda_1,j,k} \\ \Delta DPF_{\lambda_2,j,k} \\ \Delta DPF_{\lambda_3,j,k} \end{bmatrix}. \quad (11)$$

The measurement transition matrix $\mathbf{H}_{j,k}$ determines the dynamic characteristics of the model and is formed from the coefficients of ΔHbO and ΔHbR in the MBLL equation [Eq. (2)] with the addition of $\Delta DPF_{\lambda_i,j,k}$ terms that correspond to the relative changes in the differential path length factor at wavelength λ_i for source-detector pair j and time step k . $\Delta DPF_{\lambda_i,j,k}$ is updated at each time step for λ_i ($i = 690, 785, 830$) and serves as a correction term for the assumed $DPF_{\lambda_i,j}$. Three additional rows are also included in $\mathbf{H}_{j,k}$ so that we can specify statistical priors on $\Delta DPF_{\lambda_i,j,k}$:

$$\mathbf{H}_{j,k} = \begin{bmatrix} (DPF_{\lambda_{690},j} + \Delta DPF_{\lambda_{690},j,k})d_j \epsilon_{\lambda_{690},HbO} & (DPF_{\lambda_{690},j} + \Delta DPF_{\lambda_{690},j,k})d_j \epsilon_{\lambda_{690},HbR} & 0 & 0 & 0 \\ (DPF_{\lambda_{785},j} + \Delta DPF_{\lambda_{785},j,k})d_j \epsilon_{\lambda_{785},HbO} & (DPF_{\lambda_{785},j} + \Delta DPF_{\lambda_{785},j,k})d_j \epsilon_{\lambda_{785},HbR} & 0 & 0 & 0 \\ (DPF_{\lambda_{830},j} + \Delta DPF_{\lambda_{830},j,k})d_j \epsilon_{\lambda_{830},HbO} & (DPF_{\lambda_{830},j} + \Delta DPF_{\lambda_{830},j,k})d_j \epsilon_{\lambda_{830},HbR} & 0 & 0 & 0 \\ DPF_{\lambda_{808},j}d_j \epsilon_{\lambda_{808},HbO} & DPF_{\lambda_{808},j}d_j \epsilon_{\lambda_{808},HbR} & 0 & 0 & 0 \\ 0 & 0 & 1 & 0 & 0 \\ 0 & 0 & 0 & 1 & 0 \\ 0 & 0 & 0 & 0 & 1 \end{bmatrix}. \quad (12)$$

We assume that the expected values of $\Delta DPF_{\lambda_i,j,k}$ are zero. These priors are incorporated in the measurement vector $\mathbf{Y}_{j,k}$ along with $\Delta OD_{\lambda_i,j,k}$ obtained for $i = 690, 785, 808, 830$:

$$\mathbf{Y}_{j,k} = \begin{bmatrix} \Delta OD_{\lambda_{690},j,k} \\ \Delta OD_{\lambda_{785},j,k} \\ \Delta OD_{\lambda_{830},j,k} \\ \Delta OD_{\lambda_{808},j,k} \\ 0 \\ 0 \\ 0 \end{bmatrix}. \quad (13)$$

The observation model [Eq. (10)] contains an observation noise term $\mathbf{v}_{j,k}$, which is assumed to be zero mean white Gaussian noise (WGN) with covariance \mathbf{R}_j :

$$\mathbf{R}_j = \begin{bmatrix} \sigma_{\Delta OD, \lambda_{690}}^2 & 0 & \dots & 0 \\ 0 & \sigma_{\Delta OD, \lambda_{785}}^2 & & \\ & & \sigma_{\Delta OD, \lambda_{830}}^2 & \\ & & & \sigma_{\Delta OD, \lambda_{808}}^2 \\ \vdots & & & & \vdots \\ 0 & & & & \sigma_{\Delta DPF, R}^2 & 0 \\ & & \sigma_{\Delta DPF, R}^2 & 0 & \sigma_{\Delta DPF, R}^2 \end{bmatrix}. \quad (14)$$

The process model describes the dynamics of the state variables and is assumed to be stochastic:

$$\mathbf{X}_{j,k+1} = \mathbf{F}_j \mathbf{X}_{j,k} + \mathbf{w}_{j,k} \quad (15)$$

Equation (15) contains an innovation term, also known as process noise, defined in vector $\mathbf{w}_{j,k}$, that is assumed to be drawn from a zero mean multivariate normal distribution with covariance \mathbf{Q}_j :

$$\mathbf{Q}_j = \begin{bmatrix} \sigma_{\Delta HbO}^2 & 0 & \dots & 0 \\ 0 & \sigma_{\Delta HbR}^2 & & \vdots \\ \vdots & & \sigma_{\Delta DPF, Q}^2 & 0 \\ 0 & \dots & 0 & \sigma_{\Delta DPF, Q}^2 \end{bmatrix}. \quad (16)$$

The state transition matrix \mathbf{F}_j in Eq. (15) is used to describe the relationship between the state variables \mathbf{X} at time step k and $k + 1$. In our process model, \mathbf{F}_j is a 5 by 5 identity matrix.

The input and output state transition matrices \mathbf{F}_j and \mathbf{H}_j , along with the output vector $\mathbf{Y}_{j,k}$ are used in the EKF algorithm to estimate the state variables in $\mathbf{X}_{j,k}$. The EKF performs state estimation through an iterative prediction-correction scheme. In the prediction step, the most recent estimated state variables $\hat{\mathbf{X}}_{j,k-1}$ and error covariance matrix $\mathbf{P}_{j,k-1}$ are projected forward in time to compute a predicted or a prior estimate $\hat{\mathbf{X}}_{j,k}^-$ at the current time step k :

$$\hat{\mathbf{X}}_{j,k}^- = \mathbf{F}_j \hat{\mathbf{X}}_{j,k-1}. \quad (17)$$

The predicted error covariance matrix is given by:

$$\mathbf{P}_{j,k}^- = \mathbf{F}_j' \mathbf{P}_{j,k-1} \mathbf{F}_j'^T + \mathbf{Q}_j, \quad (18)$$

where \mathbf{F}_j' is the Jacobian matrix of partial derivatives of \mathbf{F}_j with respect to each of the state variables, and \mathbf{Q}_j is the process noise covariance matrix.

In the correction stage, a posterior estimate of the states $\hat{\mathbf{X}}_{j,k}$ is calculated based on a linear combination of the prior estimate $\hat{\mathbf{X}}_{j,k}^-$ and a weighted difference between the predicted measurement $\mathbf{H}_j \hat{\mathbf{X}}_{j,k}^-$ and the actual measurement $\mathbf{Y}_{j,k}$:

$$\hat{\mathbf{X}}_{j,k} = \hat{\mathbf{X}}_{j,k}^- + \mathbf{K}_{j,k} (\mathbf{Y}_{j,k} - \mathbf{H}_j \hat{\mathbf{X}}_{j,k}^-). \quad (19)$$

The optimal Kalman gain weighting matrix, $\mathbf{K}_{j,k}$, is given by:

$$\mathbf{K}_{j,k} = \mathbf{P}_{j,k}^- \mathbf{H}_j'^T (\mathbf{H}_j' \mathbf{P}_{j,k-1} \mathbf{H}_j'^T + \mathbf{R}_j)^{-1}, \quad (20)$$

where \mathbf{H}_j' is the Jacobian matrix obtained from \mathbf{H}_j . A posterior error covariance matrix, $\mathbf{P}_{j,k}$ is calculated using the predicted error covariance matrix $\mathbf{P}_{j,k}^-$:

$$\mathbf{P}_{j,k} = (\mathbf{I} - \mathbf{K}_{j,k} \mathbf{H}_j') \mathbf{P}_{j,k}^-. \quad (21)$$

The computed $\hat{\mathbf{X}}_{j,k}$ and $\mathbf{P}_{j,k}$ are then used in the next prediction step.

4 Methods

4.1 NIRS Spectroscopic Calculation with EKF Using Simulated ΔOD_λ

NIRS ΔOD_λ data was generated at 690, 785, 808, and 830 nm with a 25 Hz sampling rate using the forward equation of MBL from assumed known sequences of ΔHbO and ΔHbR . Large errors were introduced in the DPF_λ values with respect to the assumed known value of 6. We also introduced WGN such that the signal-to-noise ratio (SNR) was 40 dB. Source-detector separation distance for each of the four wavelengths was assumed to be 35 mm.

In order to use the EKF, we need to have knowledge of the variance of the measurement noise and the process noise entries in matrices \mathbf{R}_j and \mathbf{Q}_j , respectively. Measurement noise variance for the simulated data was already known from the statistics of the WGN. In the case of the measurement noise variance prior $\sigma_{\Delta\text{DPF},R}^2$ for ΔDPF_λ , we specified an upper bound of 1.31 for its value. This prior was established heuristically based on the reported standard deviation of DPF values obtained experimentally from over the somatosensory motor region.²⁵ We then

estimated the process noise variances of the state variables. The process noise variances $\sigma_{\Delta\text{HbO}}^2$ and $\sigma_{\Delta\text{HbR}}^2$ were calculated from the difference between the original ΔHbO and ΔHbR sequences and their moving averages. The moving average filter had a span of three points. The process noise variance of ΔDPF_λ , $\sigma_{\Delta\text{DPF},Q}^2$, was obtained by calculating the variance of the errors introduced in DPF_λ . We initialized the error covariance matrix $\mathbf{P}_{j,0}$ and the state variables $\mathbf{X}_{j,0}$ to zero. We then applied the EKF on the simulated ΔOD_λ data and compared the estimated time series of ΔHbO and ΔHbR with the known sequences. A weighted least squares approach (WLSQ)²⁶ was also used to estimate ΔHbO and ΔHbR for comparison with the solutions from EKF. In the WLSQ method, the measurement data was weighted by the inverse of the measurement noise variances:

$$\mathbf{W} = \begin{bmatrix} \sigma_{\Delta\text{OD},\lambda_{690}}^2 & 0 & \cdots & 0 \\ 0 & \sigma_{\Delta\text{OD},\lambda_{785}}^2 & & \vdots \\ \vdots & & \sigma_{\Delta\text{OD},\lambda_{830}}^2 & 0 \\ 0 & \cdots & 0 & \sigma_{\Delta\text{OD},\lambda_{808}}^2 \end{bmatrix}^{-1}, \quad (22)$$

where the diagonal entries of the weighting matrix \mathbf{W} correspond to the measurement noise variances for the simulated data at 690 nm, 785 nm, 830 nm and 808 nm.

4.2 Tuning the EKF Parameters Using Simulated ΔOD_λ

Inaccurate process noise variance specification can affect the convergence properties and accuracy of the EKF state estimates. In our EKF model, the parameters that required tuning were the process noise variances $\sigma_{\Delta\text{HbO}}^2$, $\sigma_{\Delta\text{HbR}}^2$, and $\sigma_{\Delta\text{DPF},Q}^2$. We estimated $\sigma_{\Delta\text{HbO}}^2$ or $\sigma_{\Delta\text{HbR}}^2$ by calculating the variance of the residual obtained by subtracting low pass filtered ΔHbO and ΔHbR sequences from the original sequences as described in the previous section. Estimating $\sigma_{\Delta\text{DPF},Q}^2$ is more challenging. In order to determine $\sigma_{\Delta\text{DPF},Q}^2$, we picked nine test values on a logarithmic scale for $\sigma_{\Delta\text{DPF},Q}^2$ ranging from 10^{-12} to 10^0 for use in the EKF with simulated NIRS data. The simulated data had errors in DPF_λ of 1.5 at 690 nm, -1.5 at 785 nm, 2.9 at 830 nm, and zero error at 808 nm so that the inaccuracies introduced are only due to cross talk. For each test value of $\sigma_{\Delta\text{DPF},Q}^2$, we calculated the mean residual sum squared (RSS) error in the estimates of ΔHbO and ΔHbR as percentages of the sum-squared total (SST). We then determined the tuned value for $\sigma_{\Delta\text{DPF},Q}^2$ as the one that produced the minimum combined percent error.

4.3 Application of the EKF Algorithm to NIRS Measurements

With the tuned EKF parameters, we ran the algorithm on actual NIRS measurements collected from three human subjects. The data were obtained from an *Institutional Review Board* (IRB) approved study in which each subject was fitted with a quad-source optode emitting light at wavelengths of 690, 785, 808, and 830 nm. The source optode was positioned on the scalp in a region over the left superior frontal lobe near position F3 on the electroencephalogram (EEG) 10 to 20 system. Data were analyzed from two detectors separated by 33 mm from the source optode. Subjects were asked to breathe normally for the first minute of the experiment to establish a baseline for processing the NIRS data in spectroscopic calculations.

Subjects were then asked to breathe normally for 2 min followed by 1 min of deep breathing. This cycle of events were repeated for 8 min. The data sampling rate was 25 Hz and noisy channels were eliminated from the study if their SNR levels were less than 0 dB. Low frequency drifts in the data were removed by fitting a 5th order polynomial to data segments with a time span of 300 s. The SNR was calculated as the ratio of the variances of low to high pass filtered ΔOD_{λ} . Low pass filtering was carried out by using a 4th order Butterworth filter with cutoff frequency at 2 Hz. The data was filtered both in the forward and reverse direction to compensate for phase lags introduced by the filter. The high pass filtered signal containing the noise components was obtained by subtracting data smoothed with a moving average filter having a time span of three points from the original detrended data.

NIRS data can also be contaminated by motion artifacts and various methods exist to remove these artifacts.²⁷ In our case, we applied Chauvenet's criterion²⁸ to reject data segments that contained motion related signal variations. A deviation ratio (DR) at each time point was calculated by dividing the ΔOD_{λ} signal deviations from their moving averages by the standard deviation of signal deviations. Signal deviations were calculated as the difference between the raw data and its smoothed version obtained by applying a moving average filter with a span of 30 points (1.2 s duration). Data with a DR greater than the standard Chauvenet's criterion threshold were eliminated and the discontinuous data segments then spliced together. The resulting motion corrected ΔOD_{λ} signals were used as input data in the EKF algorithm. We then compared ΔHbO and ΔHbR calculated using the EKF with values obtained using the WLSQ method. Results were forward and reverse filtered between 0 and 2.5 Hz with a 4th order Butterworth low-pass filter to remove high frequency noise components.

4.4 Residual Error Analysis in EKF and WLSQ

We directly quantified the percent cross-talk error in ΔHbO and ΔHbR calculated from the simulated data using EKF and WLSQ in three frequency bands that are known to contain physiologically relevant spectral peaks.²⁹ The frequency bands we designated were low frequency oscillations (LF) between 0.04 and 0.15 Hz, high frequency oscillations (HF) between 0.15 and 0.4 Hz, and cardiac oscillations (CARDIAC) between 0.4 and 2.0 Hz. First the calculated hemodynamics and the known simulation sequences were band pass filtered in forward and reverse directions in the LF, HF and CARDIAC frequency bands with 4th order Butterworth filters. These filtered signals were then subtracted from one another to give ΔHbO and ΔHbR residuals. The percentages cross-talk error in ΔHbO and ΔHbR for EKF and WLSQ were then calculated as the ratio of the standard deviations of the residuals and the known sequences in each frequency band.

In case of experimental data, we analyzed the autocorrelation structure of the residuals obtained from the EKF and WLSQ results by calculating the fraction of points outside the 95% confidence interval of the autocorrelation function. For a sample of uncorrelated residuals, one would expect that, on average, 5% of the sample autocorrelation function will lie outside this confidence interval. The first 10 s of lags were not included in the calculation to remove the contribution of the main lobe of the autocorrelation function.

We also performed cross-correlations between the residuals in the LF, HF, and CARDIAC bands. For both the EKF and

WLSQ method, we band pass filtered the corresponding residuals at each wavelength in the three frequency bands. We then cross-correlated the filtered residuals from all combinations of wavelength pairs resulting in a total of six combinations of wavelength pairs at each frequency band. These coefficients were then squared and averaged over all wavelength pairs for each source-detector pair resulting in mean squared cross-correlation coefficients. These coefficients were compared to direct measures of cross-talk error in simulation and then used as a proxy for cross talk error in the experimental NIRS data.

In order to statistically evaluate the performance of the proposed EKF algorithm, we conducted ANOVA on the EKF and WLSQ mean squared cross-correlation coefficients. First, we applied the Fisher Z-transformation³⁰ to the EKF and WLSQ mean squared correlation coefficients to obtain normally distributed random variables. These transformed variables were then used as input for the ANOVA with the factors of wavelength pair, subject, and algorithm (i.e., EKF or WLSQ).

It is not possible to obtain direct measurements of cross-talk error from experimental CW-NIRS data. Instead we computed the mean percent signal deviations between the EKF and WLSQ solutions for the ΔHbO and ΔHbR sequences to quantify the magnitude of the differences in the EKF solutions. ΔHbO and ΔHbR sequences from EKF and WLSQ were first filtered in the LF, HF, and CARDIAC bands. Each filtered sequence was then split into short segments having a span of 30 points (1.2 s duration). A residual sequence was then obtained by subtracting each EKF segment from the corresponding WLSQ segment. The percent signal deviation in ΔHbO or ΔHbR was then calculated from the ratio of standard deviations of the residual sequences and the WLSQ segments. Finally, the mean percent signal deviations in ΔHbO and ΔHbR were computed by averaging all the percent signal deviations calculated from the short segments.

5 Results

The EKF and WLSQ solutions for the simulated NIRS data are shown in Fig. 1. The solutions are displayed after low-pass filtering with a 2.5 Hz cutoff frequency using a Butterworth filter of order 4. The filter was applied both in the forward and reverse direction to compensate for phase lags introduced by the filter. Figure 1(a) shows the EKF and WLSQ solutions for ΔHbO , which agree closely with the known ΔHbO sequence as evidenced by R^2 statistics of 0.99 for EKF and 0.96 for WLSQ. The residual errors between the known ΔHbO sequence and the solution obtained using EKF and WLSQ are shown in Fig. 1(b). Similarly, Fig. 1(c) and 1(d) shows ΔHbR computed from EKF and WLSQ and their corresponding residual errors in ΔHbR . It is evident in Fig. 1(c) that ΔHbR calculated using EKF agrees almost perfectly with the known sequence ($R^2 = 0.99$). In case of WLSQ, there are large discrepancies between the calculated ΔHbR and the known sequence ($R^2 = 0.66$). We can observe from the residual error plots for EKF that the magnitude of the error decreases rapidly during the first 2 s. This is approximately the amount of time it takes for the ΔDPF_{λ} values to converge to the known values in the simulation [Fig. 1(e)]. In case of WLSQ, the residual errors do not decrease over time [Fig. 1(b) and 1(d)]; they tend to show some degree of serial correlation and contain oscillatory components.

In the simulated data, we had explicit prior knowledge of the measurement noise variance $\sigma_{\Delta OD_{\lambda}}^2$ based on the simulated WGN that was introduced in ΔOD_{λ} . The process noise variances

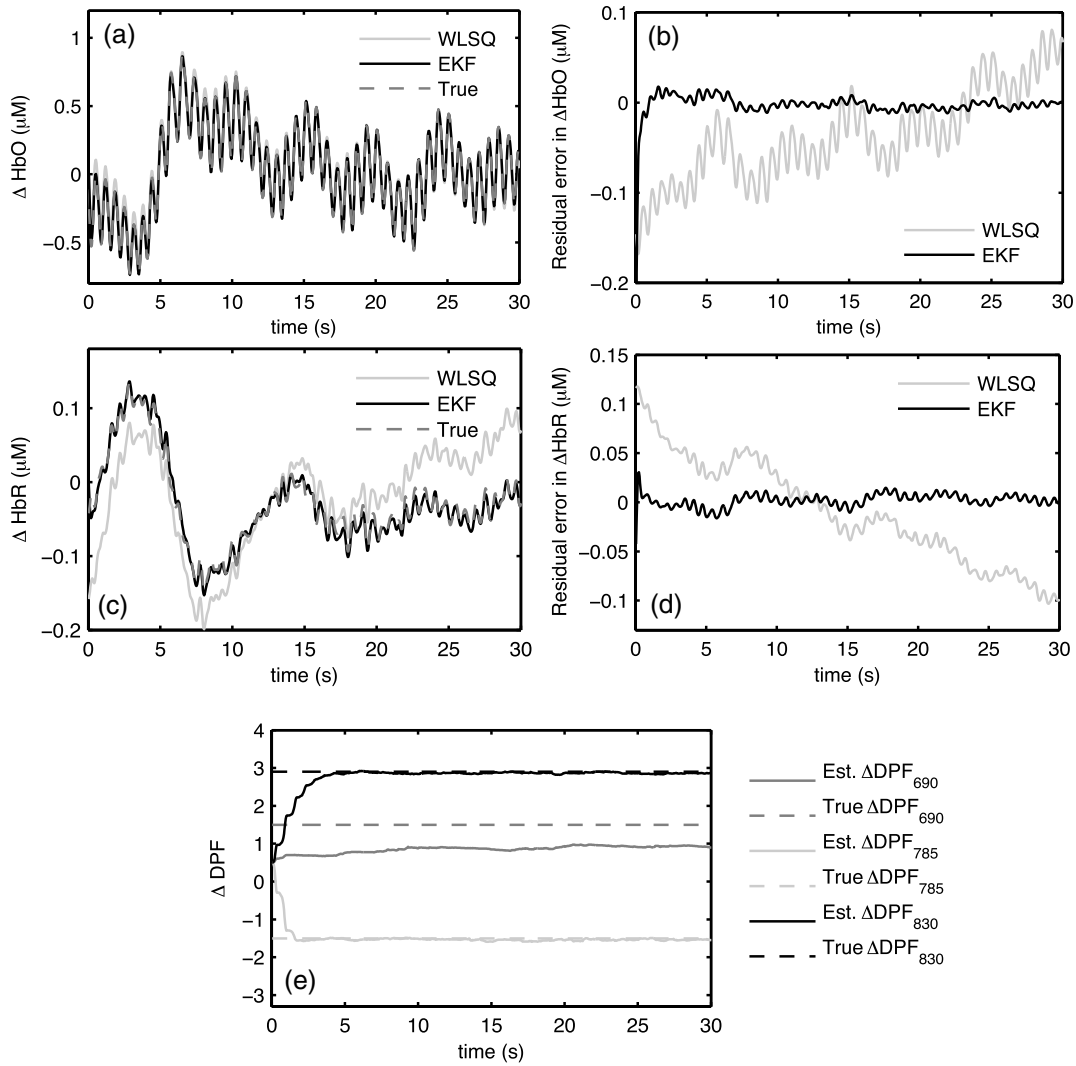


Fig. 1 EKF and WLSQ solutions for simulated NIRS data: (a) ΔHbO calculated using EKF and WLSQ and the true known sequence; (b) residual errors in ΔHbO for EKF and WLSQ; (c) ΔHbR calculated using EKF and WLSQ; (d) residual errors for ΔHbR ; (e) ΔDPF_λ terms calculated using EKF. The true ΔDPF_λ errors are shown in dotted lines.

$\sigma_{\Delta\text{HbO}}^2$ and $\sigma_{\Delta\text{HbR}}^2$ were found to be approximately $1 \times 10^{-12} (\mu\text{M})^2$. Results from tuning the process noise variance in ΔDPF_λ are shown in Fig. 2. A minimum value in the percent mean RSS error occurs at $\sigma_{\Delta\text{DPF},Q}^2 = 1 \times 10^{-6}$. This value of $\sigma_{\Delta\text{DPF},Q}^2$ was used in the EKF applied to both the simulated and experimental NIRS data.

Figure 3(a) shows the percent cross-talk error in the solutions obtained from EKF and WLSQ. The percent cross-talk error in ΔHbO is significantly smaller in EKF relative to that found for WLSQ across all frequency bands (paired t -test, $p < 0.05$). Although the cross-talk error in ΔHbR is slightly higher for EKF in the HF and CARDIAC band, the corresponding values in WLSQ are much higher at 45.9% and 35.1%, respectively.

Figure 3(b) shows the mean of the sum squared cross correlation coefficients obtained for the LF, HF, and CARDIAC frequency bands for EKF and WLSQ applied to simulated NIRS data. We can observe that the EKF has reduced mean sum squared cross-correlation coefficient values in the LF band relative to WLSQ. In case of the HF and CARDIAC bands, the mean squared cross-correlation coefficient values for EKF and WLSQ are comparable.

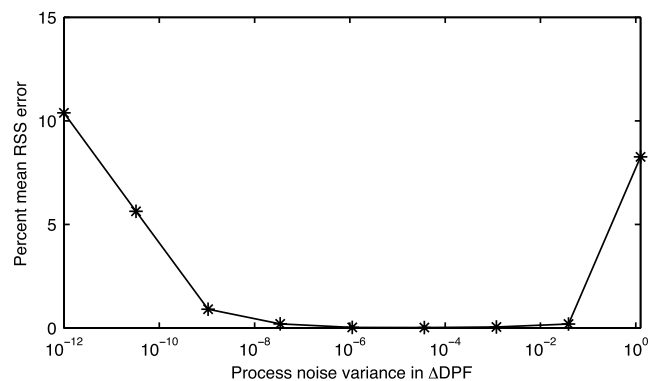


Fig. 2 Percent mean RSS error between known ΔHbO and ΔHbR and the solutions computed using EKF for nine evaluated levels of $\sigma_{\Delta\text{DPF},Q}^2$. The minimum RSS error corresponds to a process noise variance of 1×10^{-6} .

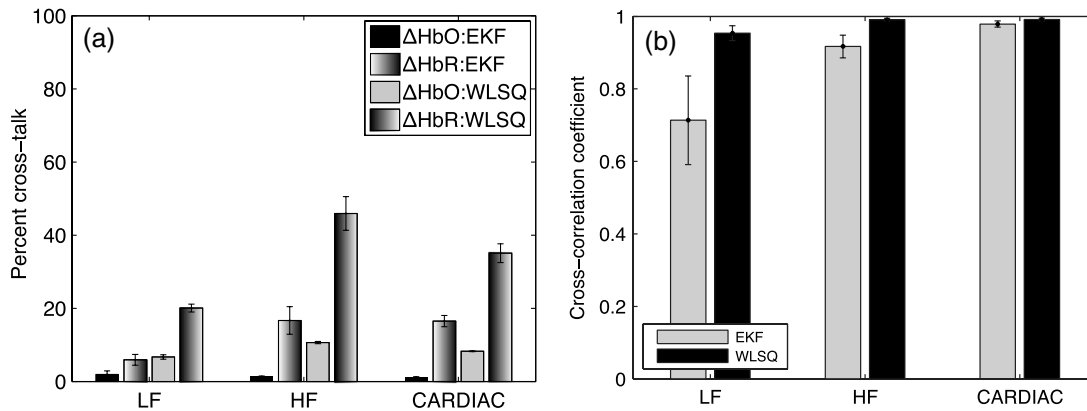


Fig. 3 Simulated NIRS data residual analysis: (a) percent cross-talk error in ΔHbO and ΔHbR solution obtained using EKF and WLSQ. Error bars show standard error; (b) mean sum squared cross-correlation coefficients for LF, HF, and CARDIAC filtered residuals for EKF and WLSQ.

The results from EKF and WLSQ applied to experimental NIRS data segments are shown in Fig. 4. ΔHbO and ΔHbR computed using EKF agree closely with the WLSQ results [Fig. 4(a) and 4(b)]. Figure 4(c) shows the ΔDPF_λ values calculated for wavelengths of 690, 785, and 830 nm. Large deviations in the ΔDPF_λ values occur between 125 and 140 s. During this time interval, the difference between the EKF and WLSQ solution for ΔHbO and ΔHbR is also large [Fig. 4(d)]. The R^2 values for the plotted time interval are 0.97 for ΔHbO and 0.98 for ΔHbR .

Figure 5 shows ΔHbO and ΔHbR results in the LF, HF and CARDIAC bands for EKF and WLSQ. The differences between the EKF and WLSQ solutions are also plotted.

Figure 6 shows the residuals obtained for WLSQ and EKF and their autocorrelation sequences for subject 3. The WLSQ and EKF residuals shown in Fig. 6(a) and 6(b) appear to contain physiological signal components such as cardiac oscillations in the EKF residuals. There also appear to be low frequency components in both the WLSQ and EKF residuals. The autocorrelation structures shown in Fig. 6(c) and 6(d) shows reduced serial correlation at larger lags in EKF compared to WLSQ. The autocorrelation values for the 690 nm residual appear to be substantially smaller in EKF compared to WLSQ.

Table 1 summarizes the mean percentages of points in the autocorrelation functions for WLSQ and EKF that fall outside

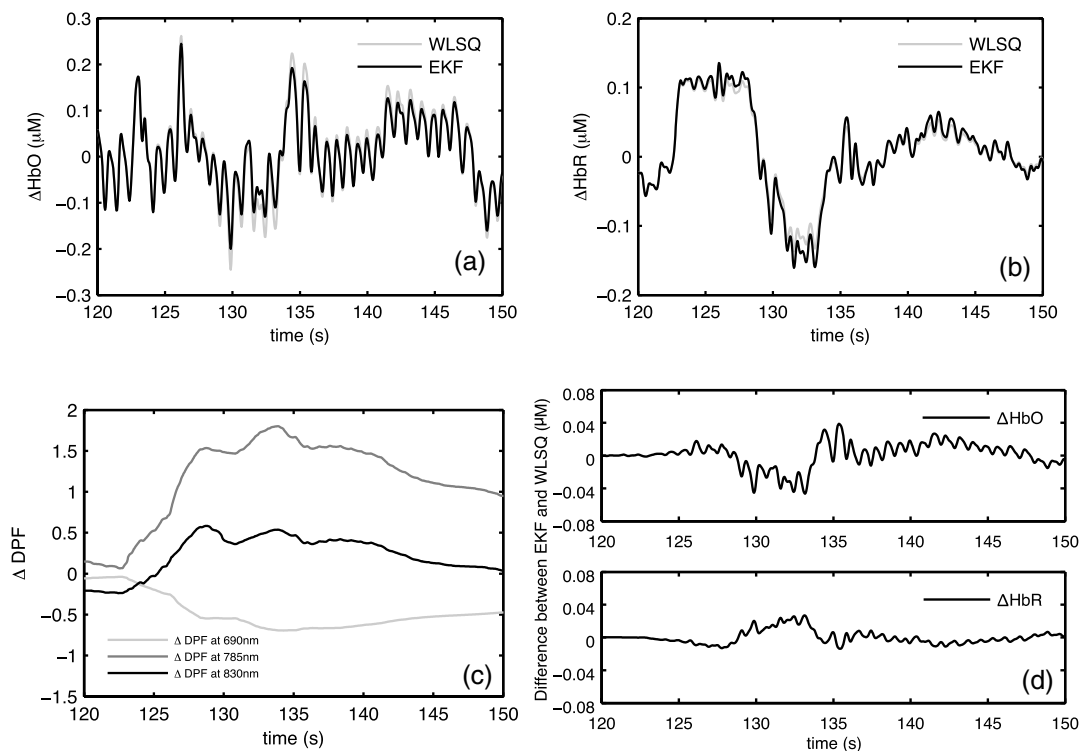


Fig. 4 EKF and WLSQ results obtained for experimental NIRS data collected from subject 3 (a) ΔHbO estimated using WLSQ and EKF (b) corresponding ΔHbR estimated using WLSQ and EKF; (c) EKF estimates of ΔDPF_λ at 690, 785, and 830 nm; (d) difference between WLSQ and EKF hemodynamic signals.

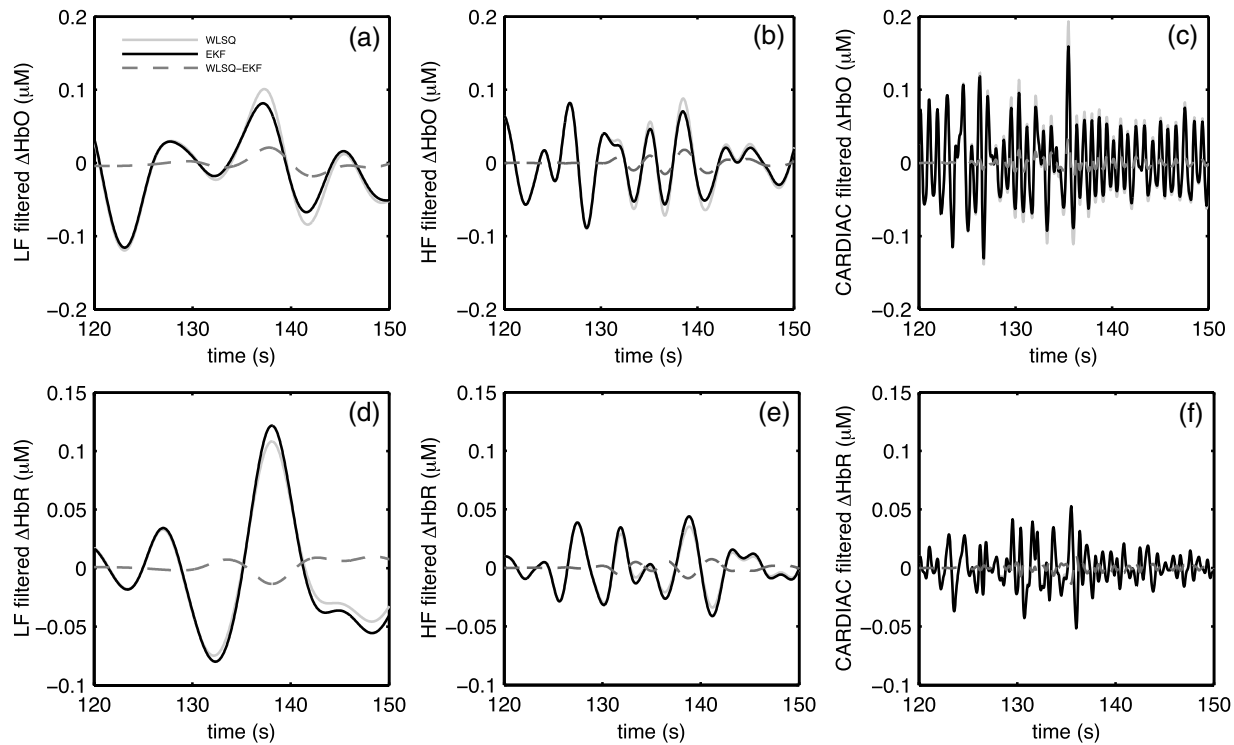


Fig. 5 Band pass filtered ΔHbO (upper row) and ΔHbR (lower row) sequences from EKF and WLSQ for subject 3: (a) and (d) LF (0.04 to 0.15 Hz); (b) and (e) HF (0.15 to 0.4 Hz); (c) and (f) CARDIAC (0.4 to 2.0 Hz).

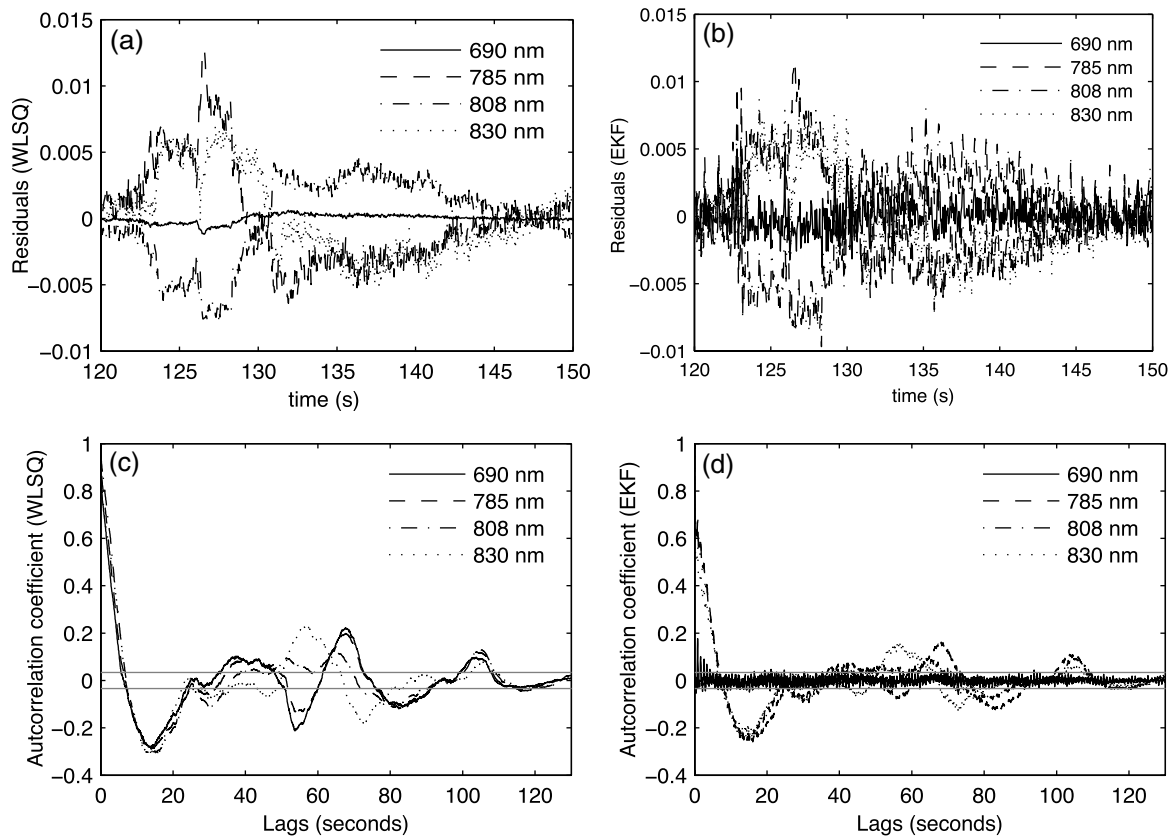
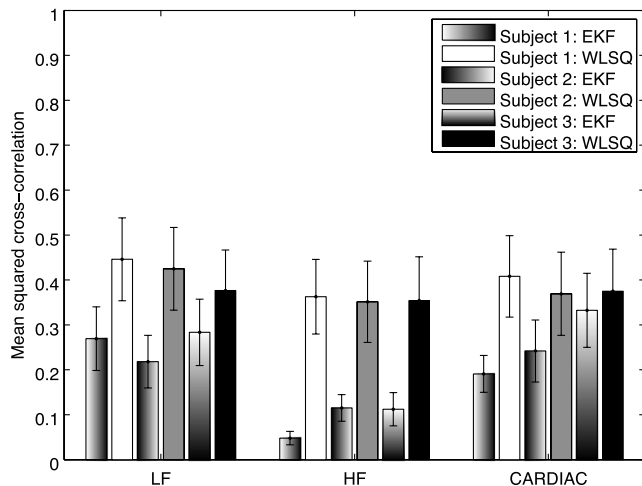


Fig. 6 (a) WLSQ residuals for wavelengths 690, 758, 808, and 830 nm; (b) EKF residuals for the four wavelengths; (c) autocorrelation coefficients for residuals from WLSQ with the 95% confidence interval shown in solid gray lines (d) autocorrelation coefficient of residuals from EKF with the 95% confidence interval shown in solid gray lines.

Table 1 Mean percentages of points that fall outside of the 95% confidence intervals for the EKF and WLSQ autocorrelation functions.

Wavelength (nm)	WLSQ (%)	EKF (%)
690	39.6	4.1
785	41.9	34.4
808	41.1	29.2
830	38.4	21.7

**Fig. 7** Mean squared cross-correlation coefficients of residuals from the analysis of experimental data from three subjects. Results are shown for LF, HF and CARDIAC frequency bands with standard error bars.

of the 95% confidence intervals. The percentages of points outside the confidence bounds for EKF are consistently smaller than for WLSQ.

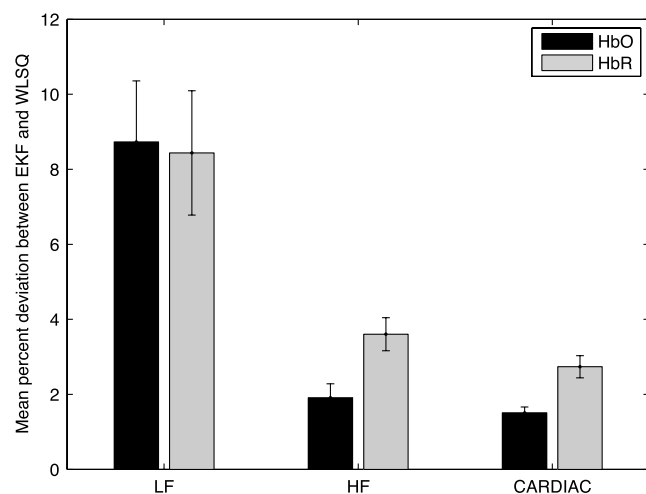
Figure 7 compares the mean squared cross-correlation coefficient values obtained in the analysis of EKF and WLSQ residuals. All three subjects have smaller mean squared correlation coefficient values for EKF relative to those found for WLSQ (see Table 2 for ANOVA). The lowest mean squared cross-correlation coefficients were found for the HF band in EKF.

ANOVA results are summarized in the Table 2. Algorithm (EKF versus WLSQ) contributes significantly ($p < 0.001$) in all three frequency bands. Therefore, we can reject the null hypothesis that the mean squared cross-correlation coefficient values found for EKF and WLSQ are the same at those frequency bands. It is interesting to note that the wavelength factor also contributes significantly to the variability in the mean squared cross-correlation coefficient values indicating that the EKF corrections vary significantly with wavelength.

Figure 8 shows the mean percent deviations between EKF and WLSQ solutions in the LF, HF and CARDIAC frequency bands. For each frequency band, the mean percent deviations in ΔHbO and ΔHbR are significantly different from zero (two-tailed t -test: $p < 0.001$). The mean deviation over all frequency bands was found to be 4.04% for ΔHbO and 4.92% for ΔHbR . In the LF band, the mean percent deviations are comparable for both ΔHbO and ΔHbR . The mean percent signal deviation is

Table 2 NOVA of mean squared cross-correlation values shown in Fig. 7.

Factor	Sum Sq.	d.f.	Mean Sq.	F	P-value
LF (0.04–0.15 Hz)					
Wavelength	6.060	5	1.212	7.39	<0.001
Subject	0.027	2	0.013	0.08	0.9217
Algorithm	2.400	1	2.400	14.63	<0.001
Error	10.34	63	0.164		
Total	18.82	71			
LF (0.04–0.15 Hz)					
Wavelength	6.499	5	1.299	10.90	<0.001
Subject	0.269	2	0.134	1.13	0.3289
Algorithm	1.415	1	1.415	11.87	<0.001
Error	7.512	63	0.119		
Total	15.697	71			
CARDIAC (0.4–2.0 Hz)					
Wavelength	5.329	5	1.065	12.83	<0.001
Subject	0.002	2	0.001	0.01	0.9863
Algorithm	2.699	1	2.699	32.49	<0.001
Error	5.234	63	0.083		
Total	13.27	71			

**Fig. 8** Mean percent deviations between EKF and WLSQ solutions filtered in the LF, HF, and CARDIAC frequency bands shown with 95% confidence intervals from a paired t -test.

smaller in ΔHbO compared to ΔHbR in the HF and CARDIAC bands ($p < 0.05$).

6 Discussion and Conclusion

The proposed EKF algorithm is able to calculate ΔHbO and ΔHbR from simulated NIRS data by continuously updating ΔDPF_λ values. We observed in simulation that the residual errors in ΔHbO and ΔHbR decrease rapidly within the first 2 s as the EKF tracked the errors introduced in DPF_λ . In the analysis of experimental data, we observed reduced autocorrelation of residuals for EKF compared to WLSQ. We believe that the superior performance of EKF is achieved due to weighting of the state variable innovations by the optimal Kalman gain at each time step. The application of the Kalman gain in this way helps to minimize the posterior error covariance over time. In WLSQ, the measurement data is weighted by constant factors over all time steps; so even though the solution is optimal in the least squares sense, WLSQ lacks the flexibility of EKF to account for time variation in DPF_λ . As a result, EKF outperforms WLSQ in the estimation of ΔHbO and ΔHbR .

We observed reduced cross-correlations in the residuals in wavelength pairs for EKF in the LF, HF and CARDIAC bands compared to WLSQ, which is consistent with the reduction of cross-talk error. Convergence of the EKF state estimates to the true states is dependent on prior knowledge of the process noise and measurement noise variance statistics. In the proposed method, we demonstrate how to obtain prior estimates of those statistics based on minimizing the residual error in EKF.

We also quantified the differences in the hemodynamic signals calculated using EKF and WLSQ in physiologically relevant frequency bands. We found significant differences in the ΔHbR sequences in the LF and HF bands. The average of differences between EKF and WLSQ solutions across all frequency bands was 3.75% for ΔHbO and 4.57% for ΔHbR . We believe that this difference is due to a reduction of cross-talk error in ΔHbO and ΔHbR obtained using EKF. This is supported by the observation that the EKF solution obtained from simulated NIRS data had reduced cross-talk error relative to the WLSQ solutions. In the simulation, the errors in ΔHbO and ΔHbR from the known sequences were significantly lower in the EKF results compared to the WLSQ results.

The proposed EKF method offers several advantages over other methods that may be used to calculate DPF_λ . Unlike other studies where DPF_λ is estimated based on the assumption that it is constant over time,^{2,25,31} the proposed EKF algorithm continuously updates DPF_λ and it can account for variation in DPF_λ due to differences in anatomical structure and tissue composition of the brain. In cases where relative calibration of ΔHbO and ΔHbR is desired, the proposed method eliminates the need to measure DPF_λ using TD or FD instruments or applying simulation techniques discussed in Sec. 2.

The proposed EKF algorithm has potential applications in the clinical investigation of brain injury. A number of recent studies have used NIRS to monitor patients during stroke rehabilitation and recovery.^{32–34} A limitation in these studies is the inability to accurately quantify cerebral hemodynamics in a region of interest. In the above referenced stroke studies, DPF_λ is assumed to be constant over time and the studies did not account for possible variation due to the stroke. However, DPF_λ could deviate substantially in stroke because of the high absorption coefficient of hemoglobin. As a result, the calculated ΔHbO and ΔHbR may not have accurately

reflected the hemodynamics in those patients. The proposed algorithm could also be applied to other clinical diagnostic applications of NIRS such as breast cancer detection.³⁵ The optical properties of cancerous tissue are different from those of healthy tissue in the breast. Accurate assessment of hemodynamic changes in breast tissue also relies on using accurate estimates of DPF in the NIRS spectroscopic calculations. Further investigation is required to determine if the proposed EKF algorithm is able to correct path length errors in NIRS applications in stroke, cancer, and other clinical conditions.

References

1. D. T. Delpy and M. Cope, "Quantification in tissue near-infrared spectroscopy," *Phil. Trans. R. Soc. Lond. B* **352**(1354), 649–659 (1997).
2. A. Duncan et al., "Optical pathlength measurements on adult head, calf and forearm and the head of the newborn infant using phase resolved optical spectroscopy," *Phys. Med. Biol.* **40**(2), 295–304 (1995).
3. D. T. Delpy et al., "Estimation of optical pathlength through tissue from direct time of flight measurement," *Phys. Med. Biol.* **33**(12), 1433–1442 (1988).
4. J. Selb, D. K. Joseph, and D. A. Boas, "Time-gated optical system for depth-resolved functional brain imaging," *J. Biomed. Opt.* **11**(4), 044008 (2006).
5. B. R. White and J. P. Culver, "Quantitative evaluation of high-density diffuse optical tomography: in vivo resolution and mapping performance," *J. Biomed. Opt.* **15**(2), 026006 (2010).
6. M. A. Franceschini et al., "Diffuse optical imaging of the whole head," *J. Biomed. Opt.* **11**(5), 054007 (2006).
7. M. Cope et al., "Methods of quantitating cerebral near infrared spectroscopy data," *Adv. Exp. Med. Biol.* **222**, 183–189 (1988).
8. J. S. Ulman and C. A. Piantadosi, "Differential pathlength factor for diffuse photon scattering through tissue by a pulse-response method," *Math. Biosci.* **107**(1), 73–82 (1991).
9. C. Bonneré et al., "Changes in diffusion path length with old age in diffuse optical tomography," *J. Biomed. Opt.* **17**(5), 056002 (2012).
10. G. Strangman, M. A. Franceschini, and D. A. Boas, "Factors affecting the accuracy of near-infrared spectroscopy concentration calculations for focal changes in oxygenation parameters," *NeuroImage* **18**(4), 865–879 (2003).
11. K. Yoshitani et al., "Effects of hemoglobin concentration, skull thickness, and the area of the cerebrospinal fluid layer on near-infrared spectroscopy measurements," *Anesthesiology* **106**(3), 458–462 (2007).
12. E. Okada and D. T. Delpy, "Near-infrared light propagation in an adult head model. I. Modeling of low-level scattering in the cerebrospinal fluid layer," *Appl. Opt.* **42**(16), 2906–2914 (2003).
13. D. A. Benaron, C. D. Kurth, and J. M. Steven, "Transcranial optical path length in infants by near-infrared phase-shift spectroscopy," *J. Clin. Monit.* **11**(2), 109–117 (1995).
14. K. Yoshitani et al., "Measurements of optical pathlength using phase-resolved spectroscopy in patients undergoing cardiopulmonary bypass," *Anesth. Analg.* **104** (2), 341–346 (2007).
15. S. Muehlschlegel et al., "Feasibility of NIRS in the neurointensive care unit: a pilot study in stroke using physiological oscillations," *Neurocrit. Care* **11**(2), 288–295 (2009).
16. M. N. Kim et al., "Noninvasive measurement of cerebral blood flow and blood oxygenation using near-infrared and diffuse correlation spectroscopies in critically brain-injured adults," *Neurocrit. Care* **12**(2), 173–180 (2010).
17. Y. Oki, H. Kawaguchi, and E. Okada, "Validation of practical diffusion approximation for virtual near infrared spectroscopy using a digital head phantom," *Opt. Rev.* **16**(2), 153–159 (2009).
18. F. Gao, H. Niu, and H. Zhao, "The forward and inverse models in time-resolved optical tomography imaging and their finite-element method solutions," *Image Vis. Comput.* **16**(9), 703–712 (1998).
19. S. R. Arridge, M. Cope, and D. T. Delpy, "The theoretical basis for the determination of optical pathlengths in tissue: temporal and frequency analysis," *Phys. Med. Biol.* **37**(7), 1531–1560 (1992).
20. Y. Fukui, Y. Ajichi, and E. Okada, "Monte Carlo prediction of near-infrared light propagation in realistic adult and neonatal head models," *Appl. Opt.* **42**(16), 2881–2887 (2003).

21. E. Okada et al., "Theoretical and experimental investigation of near-infrared light propagation in a model of the adult head," *Appl. Opt.* **36**(1), 21–31 (1997).
22. K. Uludag et al., "Cross talk in the Lambert-Beer calculation for near-infrared wavelengths estimated by Monte Carlo simulations," *J. Biomed. Opt.* **7**(1), 51–59 (2002).
23. M. Hiraoka et al., "A Monte Carlo investigation of optical pathlength in inhomogeneous tissue and its application to near-infrared spectroscopy," *Phys. Med. Biol.* **38**(12), 1859–1876 (1993).
24. N. Okui and E. Okada, "Wavelength dependence of crosstalk in dual-wavelength measurement of oxy- and deoxy-hemoglobin," *J. Biomed. Opt.* **10**(1), 011015 (2005).
25. H. Zhao et al., "Maps of optical differential pathlength factor of human adult forehead, somatosensory motor and occipital regions at multi-wavelengths in NIR," *Phys. Med. Biol.* **47**(12), 2075–2093 (2002).
26. T. J. Huppert et al., "HomER: a review of time-series analysis methods for near-infrared spectroscopy of the brain," *Appl. Opt.* **48**(10), D280–D298 (2009).
27. F. C. Robertson, T. S. Douglas, and E. M. Meintjes, "Motion artifact removal for functional near infrared spectroscopy: a comparison of methods," *IEEE Trans. Biomed. Eng.* **57** (6), 1377–1387 (2010).
28. J. P. Holman, *Experimental Methods for Engineers*, 4th ed., McGraw-Hill Inc., New York (1984).
29. A. Camm et al., "Heart rate variability-Standards of measurement, physiological interpretation, and clinical use," *Circulation* **93**(5), 1043–1065 (1996).
30. R. A. Fisher, "On the 'probable error' of a coefficient of correlation deduced from a small sample," *Metron* **1**(4), 3–32 (1921).
31. S. Umeyama, "New method of estimating wavelength-dependent optical path length ratios for oxy- and deoxyhemoglobin measurement using near-infrared spectroscopy," *J. Biomed. Opt.* **14**(5), 054038 (2009).
32. G. Strangman et al., "Near-infrared spectroscopy and imaging for investigating stroke rehabilitation: test-retest reliability and review of the literature," *Arch. Phys. Med. Rehabil.* **87**(12), 12–19 (2006).
33. J. C. Eliassen et al., "Brain-mapping techniques for evaluating poststroke recovery and rehabilitation: a review," *Top. Stroke Rehabil.* **15**(5), 427–450 (2008).
34. P. Y. Lin et al., "Review: applications of near infrared spectroscopy and imaging for motor rehabilitation in stroke patients," *J. Med. Biol. Eng.* **29**(5), 210–221 (2009).
35. S. Fantini and A. Sassaroli, "Near-infrared optical mammography for breast cancer detection with intrinsic contrast," *Ann. Biomed. Eng.* **40**(2), 398–407 (2012).